RESEARCH ARTICLE
SOLID EARTH: GEODESY AND GRAVITY

Earth and Planetary Physics
6: 366–377, 2022
doi: 10.26464/epp2022034

Vertical crustal deformation velocity and its influencing factors over the Qinghai–Tibet Plateau based on satellite gravity data

HuRong Duan[1,4*], JunGang Guo[1], LingKang Chen[2,5], JiaShuang Jiao[3], and HeTing Jian[1]

[1]College of Geomatics, Xi'an University of Science and Technology, Xi'an 710054, China;

[2]College of Sciences, Guangdong University of Petrochemical Technology, Maoming Guangdong 525000, China;

[3]School of Geodesy and Geomatics, Wuhan University, Wuhan 430072, China;

[4]State Key Laboratory of Geodesy and Earth's Dynamics, Innovation Academy for Precision Measurement Science and Technology, Chinese Academy of Sciences, Wuhan 430077, China;

[5]School of Resource and Environmental Engineering, Jiangxi University of Science and Technology, Ganzhou Jiangxi 341000, China

Key Points:

- Annual gravity change rates on the Tibetan Plateau (TP) caused by tectonic movement were obtained from gravity recovery and climate experiment (GRACE) observations.
- A model of gravity changes caused by vertical crustal movements was established, and the rate of vertical crustal deformation over the Tibetan Plateau was inverted.
- The effects of hydrological factors on the vertical crustal motion rate were determined.

Citation: Duan, H. R., Guo, J. G., Chen, L. K., Jiao, J. S., and Jian, H. T. (2022). Vertical crustal deformation velocity and its influencing factors over the Qinghai–Tibet Plateau based on satellite gravity data. *Earth Planet. Phys.*, *6*(4), 366–377. http://doi.org/10.26464/epp2022034

Abstract: The uplift of the Qinghai–Tibet Plateau (TP) strongly influences climate change, both regionally and globally. Surface observation data from this region have limited coverage and are difficult to obtain. Consequently, the vertical crustal deformation velocity (VCDV) distribution of the TP is poorly constrained. In this study, the VCDV from the TP was inverted by using data from the gravity recovery and climate experiment (GRACE). We were able to obtain the vertical crustal movement by deducting the hydrological factors, based on the assumption that the gravity signal detected by GRACE is mainly composed of hydrological factors and vertical crustal movement. From the vertical crustal movement, we inverted the distribution of the VCDV across the TP. The results showed that the VCDV of the southern, eastern, and northern TP is ~1.1 mm/a, ~0.5 mm/a, and −0.1 mm/a, respectively, whereas that of the region between the Qilian Haiyuan Fault and the Kunlun Fault is ~0.0 mm/a. These results are consistent with the distribution of crustal deformation, thrust earthquakes and faults, and regional lithospheric activity. The hydrology, crustal thickness, and topographic factors did not change the overall distribution of the VCDV across the TP. The influence of hydrological factors is marked, with the maximum differences being approximately −0.4 mm/a in the northwest and 1.0 mm/a in the central area. The results of this study are significant for understanding the kinematics of the TP.

Keywords: GRACE (gravity recovery and climate experiment); Qinghai–Tibet Plateau; crustal vertical deformation; hydrological factors; crustal thickness

1. Introduction

The uplift of the Qinghai–Tibet Plateau (TP) has a strong impact on the regional and global climate and is closely related to persistent drought, earthquakes, landslides, and other natural disasters that frequently occur in the interior of Asia. Consequently, it is of great scientific significance to study the vertical crustal deformation velocity (VCDV) distribution of the TP (An ZS et al., 2001; Dai FC et al., 2011). The TP was formed by collision (and subsequent compression) between the Indian and Eurasian plates and can be explained by the theories of "crustal shortening and thickening" (Dewey and Burke, 1973), "convective removal of the lithospheric mantle" (England and Molnar, 1990), "lithospheric thickening and delamination" (Molnar and Tapponnier, 1975), and "asthenosphere upwelling bottom invasion" (He CS, 2019).

In recent years, global positioning system (GPS) and leveling techniques have been used to study crustal tectonic movements of the TP. Using GPS technology, Wang Q et al. (2001) found that the deformation within the TP and its southern margin absorbed more than 90% of the relative motion between the Indian plate and Eurasian plate. The VCDV in the Himalayas is ~2.0 mm/a (Liang SM et al., 2013), the uplift rate in the middle-eastern areas of the TP is 1.0–2.0 mm/a (Liang SM et al., 2013) or 2.7 ± 0.3 mm/a (Yi S et al., 2016), and the uplift rate at the Lhasa station in the

Correspondence to: H. R. Duan, duanhurong126@xust.edu.cn
Received 11 FEB 2022; Accepted 17 APR 2022.
Accepted article online 27 MAY 2022.

middle-southern area of the TP is approximately 0.8 ± 0.5 mm/a (Sun WK et al., 2009) or 1.4 ± 0.1 mm/a (Xing LL et al., 2011). Using a combination of GPS and precision leveling technologies, Hao M et al. (2014) found that most regions of the eastern margin of the TP are in the status of uplift and that the maximum uplift has reached 6.0 ± 1.3 mm/a. By a combination of GPS and gravity recovery and climate experiment (GRACE) techniques, Pan YJ et al. (2018) found that the average VCDV is ~1.7 mm/a in the Himalayan region and ~1.3 mm/a in the northeast of the TP. After removing the glacial isostatic adjustment (GIA) effect and the loading deformation of hydrology from the GPS data, Jiao JS et al. (2019) obtained uplift rates of 1.2 ± 0.5 mm/a and 1.1 ± 0.4 mm/a for the western and central regions of the TP, respectively. These previous studies provide abundant data for understanding the vertical crustal deformation of the TP. However, owing to harsh natural conditions (e.g., topography, geomorphology), the TP has few ground survey sites and, consequently, few observational data sets, making it difficult to obtain the spatial distribution of the VCDV.

The GRACE data can provide high-precision, high-resolution observations with which to study the global gravity field distribution (Rao WL and Sun WK, 2022; Shen Y et al.,2022). These data have been widely used in studies of hydrology (Mohamed et al., 2017), seismology (Han SC et al., 2006), ice sheet mass loss (Velicogna, 2009), and crustal tectonic movements (Duan HR et al., 2020). An earlier inversion using GRACE data provided a crustal uplift rate of ~10.0 mm/a in the Himalayas (Duan HR et al., 2011), which was close to that of 8.0 to 9.0 mm/a provided by three-dimensional finite element numerical simulations (Li P et al., 2012). After deducting the gravity effects of the GIA and hydrology from the GRACE data, Duan HR et al. (2020) obtained an uplift rate in the Himalayan region of 2.0 ± 0.9 mm/a.

Various topographical, hydrological, and crustal factors should be considered when studying the VCDV of the TP because the topography of the TP is high in the west and low in the east, with large gradient changes and height differences of 200–600 m, accounting for 59.15% of the total area (Feng ZM et al., 2020). The average altitude exceeds 4,000 m, and the TP has a large number of glaciers, snow-covered areas, lakes, and other water bodies in its interior, all of which are sensitive to climate change. The second Chinese national glacier inventory showed that the total surface area of some 24,300 glaciers has decreased by 17% (Qiu J, 2010), that the total area volume of lake water above 10 km^2 on the TP had increased by 117.1 billion m^3 from 1976 to 2013 (Qiao BJ et al., 2019), and that the snow cover ratio on the TP had increased slightly by approximately 0.16‰/a from 2000 to 2019 (Ye H et al., 2020). Owing to the collision and compression of the Indian plate, strong tectonic activity has occurred on the TP since the Late Cenozoic, forming a series of active faults that have led to frequent earthquakes (Figure 1). The Moho surface in the interior of the TP is relatively flat but undulating on the periphery. The Moho depth increases from ~30 km in India to ~80 km in the Himalayas and decreases from ~70 km in the Bangong–Nujiang suture zone to ~45–50 km in the Tarim Basin (Braitenberg et al., 2000).

Despite the TP attracting much research attention, incomplete consideration of the hydrology, crustal thickness, and topographic factors has hampered investigations of vertical crustal deformation on the TP, and its spatial distribution remains poorly understood. In this study, we used GRACE signals to invert the VCDV distribution of the TP based on the assumption that the data consist of vertical

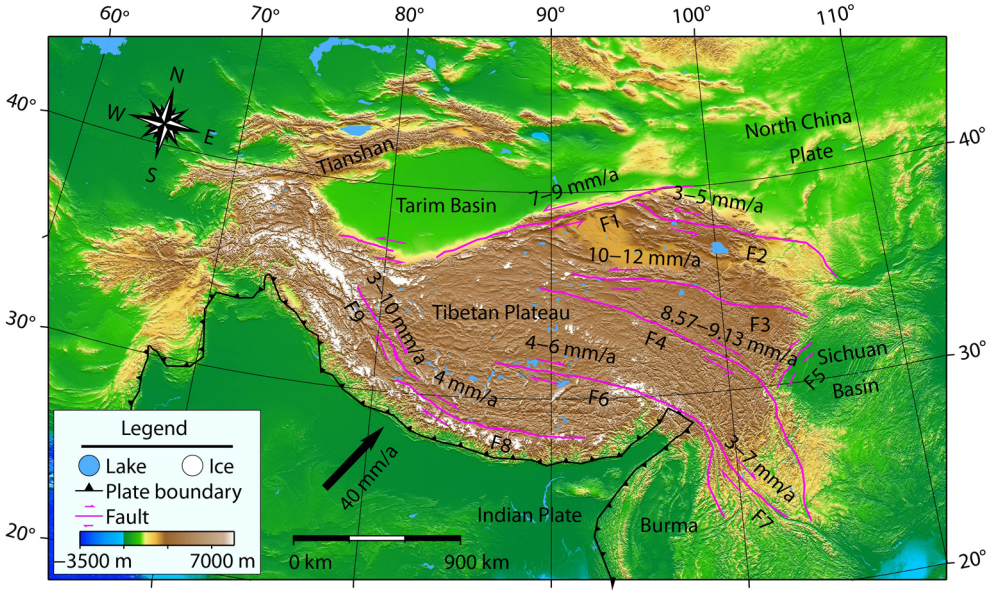

Figure 1. Distribution of fault structures in the Qinghai–Tibet Plateau (TP) and neighboring areas. The thick black line with triangles represents the boundary between the Indian plate and the Eurasian plate. The thick magenta lines indicate the main fault zones in the TP region (Duan HR et al., 2020). The bright blue patches represent lakes, and the white patches represent glaciers. The thick black arrow indicates the velocity at which the Indian plate is squeezing the Eurasian plate. F1, Altun Fault Zone; F2, Qilian–Haiyuan Fault Zone; F3, Kunlun Fault Zone; F4, Xianshui River Fault Zone; F5, Longmenshan Fault Zone; F6, Bangongcuo–Jiali Fault Zone; F7, Red River Fault Zone; F8, Himalayan active belt; F9, Karakorum Fault Zone. The horizontal axis is longitude and the vertical axis is latitude; the same as follow.

crustal movements and hydrological factors. The results provide a new perspective for understanding the kinematics of the TP.

2. Data and Methods

2.1 Gravity Change Rate of Vertical Crustal Movement Extracted from GRACE Data

2.1.1 Calculation of the gravity change rate by using GRACE data

In this research, we used the RL06 GRACE data of order/degree 60 from 2005 to 2020 published by the University of Texas Center for Space Research (UTCSR), the German Research Centre for Geosciences (GFZ), and the National Aeronautics and Space Administration (NASA) Jet Propulsion Laboratory (JPL). The geocentric terms (degree one coefficients) were provided by Sun Y et al. (2016), and the degree two coefficients were replaced with satellite laser ranging (SLR; Loomis et al., 2020). The combination of decorrelation filter (For example, for spherical harmonic (SH) coefficient of order 6 (e. g., $C_{n,6}$, $n = 6, 7, \cdots, 60$), we fit a degree 4 polynomial to the even degree pair (e.g., $C_{6,6}, C_{8,6}, \cdots, C_{60,6}$) and remove the polynomial fit from the coefficients, and apply the same to the odd degree pair (e.g., $C_{7,6}, C_{9,6}, \cdots, C_{59,6}$); P4M6) and Gaussian filtering (300 km) was used to weaken the north–south strip noise and suppress the high-frequency noise (Chen JL et al., 2010). The GIA effect was then deducted by using the GIA model (spatial resolution: 1° × 1°) of Geruo et al. (2013). The least-squares algorithm was used to calculate the gravity change rate (Steffen et al., 2009), and forward modeling was used for signal recovery (Chen JL et al., 2015).

2.1.2 Calculation of the gravity change rate by using hydrological data

Hydrological factors mainly included glaciers, soil moisture (SM), lakes, denudation, permafrost, snow water equivalent (SWE), and groundwater. Among them, SM data were from the Climate Prediction Center (CPC) soil moisture models (spatial resolution: 0.5° × 0.5°) from 2005 to 2020, SWE data were from the Global Land Data Assimilation System (GLDAS) land water models (spatial resolution: 1° × 1°) from 2005 to 2020 (Rodell et al., 2004; Rao WL and Sun WK, 2021), glacial data were from the average elevation change of glaciers from 2003 to 2009 (Gardner et al., 2013), lake data were from NASA's Ice, Cloud, and land Elevation satellite (ICESat) data from 2003 to 2009 (Zhang GQ et al., 2011), permafrost data were from an active-layer depth model from 1980 to 2001 (Oelke and Zhang TJ, 2007; Erkan et al., 2011; Xiang LW et al., 2016), and denudation data were from Westaway's (1995) estimation of the amount of denudation on the TP. Given the uneven distribution, insufficient depth, and inadequate coverage of groundwater logging data in the TP region, the monitoring results do not accurately reflect the actual groundwater situation; therefore, the influence of groundwater was not considered in this research. Although the time spans of the various observations differed, the long-term trends of these observations were linear and could be used to calculate the gravity change rate of hydrologic factors. To calculate the rate of gravity change attributable to hydrological factors, various hydrological data were converted into 60 order/degree harmonic coefficients by the methods of Xiang LW et al. (2016) and Wang HS et al. (2006) to obtain data of the same order/degree as the GRACE. Thereafter, Gaussian filtering (300 km) and signal recovery were performed.

2.1.3 Gravity change rate attributable to vertical crustal movement

We assumed that GRACE signals mainly consisted of vertical crustal movement and hydrological factors. Thus, to obtain the gravity change attributable to vertical crustal movement, it was necessary to deduct the gravity change attributable to hydrological factors, including glaciers, lakes, SM, permafrost, denudation, and SWE. The relationships among the observations and physical variables can be described as follows:

$$V_{\mathrm{GRACE}} = V_{\mathrm{Hydrological}} + V_{\mathrm{Vertical\ crustal\ movement}}, \quad (1)$$

$$V_{\mathrm{Hydrological}} = V_{\mathrm{Lake}} + V_{\mathrm{Glacier}} + V_{\mathrm{SWE}} + V_{\mathrm{SM}} + V_{\mathrm{Permafrost}} + V_{\mathrm{Denudation}}, \quad (2)$$

where V_{GRACE} is the GRACE observed gravity change rate, $V_{\mathrm{Hydrological}}$ is the rate of gravity change attributable to hydrological factors, $V_{\mathrm{Vertical\ crustal\ movement}}$ is the rate of gravity change attributable to vertical crustal movement, V_{Lake} is the rate of gravity change attributable to lakes, V_{Glacier} is the rate of gravity change attributable to glaciers, V_{SWE} is the rate of gravity change attributable to SWE, V_{SM} is the rate of gravity change attributable to SM, $V_{\mathrm{Permafrost}}$ is the rate of gravity change attributable to permafrost, and $V_{\mathrm{Denudation}}$ is the rate of gravity change attributable to denudation.

2.2 Numerical Simulation of Signal Data Processing

Truncation, spherical harmonic expansion, filtering, and signal recovery were used in the processing of GRACE data and hydrological data. To determine the loss rate of the above methods on the signal and the effectiveness of the signal recovery methods, we conducted numerical simulation experiments.

First, the TP region was divided into 1° × 1° grids, and the gravity signal of each grid was assumed to be 10 μGal, which was regarded as the true signal (Figure 2a). A 60 order/degree spherical harmonic expansion was carried out to recalculate the gravity signal (Figure 2b), and the results accounted for 98.5% of the area shown in Figure 2a. The true signal spherical harmonic expansion truncated to 60 order/degree was obtained by Gaussian filtering (300 km; Figure 2c) and accounted for 91.3% of the area shown in Figure 2a. Then P4M6 and Gaussian filtering (300 km) were applied to the results shown in Figure 2b to obtain the true signal spherical harmonic expansion truncated to 60 order/degree (Figure 2d), which accounted for 86.9% of the area shown in Figure 2a. From the difference between Figure 2c and Figure 2d, we obtained the influence of P4M6 filtering (Figure 2e), which accounted for 4.4% of the area shown in Figure 2a. The signal loss rate after P4M6 filtering was relatively small.

To verify the effectiveness of the signal recovery method, we used the data shown in Figure 2c as the input signal and used forward modeling for signal recovery. After 30 iterations, the recovered model signal (Figure 2f) accounted for 96.3% of the true signal (Figure 2a), confirming that this recovery method was able to recover the signal effectively. Gaussian filtering (300 km) was performed on the model signal (Figure 2f) to obtain a grid of the model signal's spherical harmonic expansion truncated to 60 order/degree (Figure 2g), which accounted for 91.3%

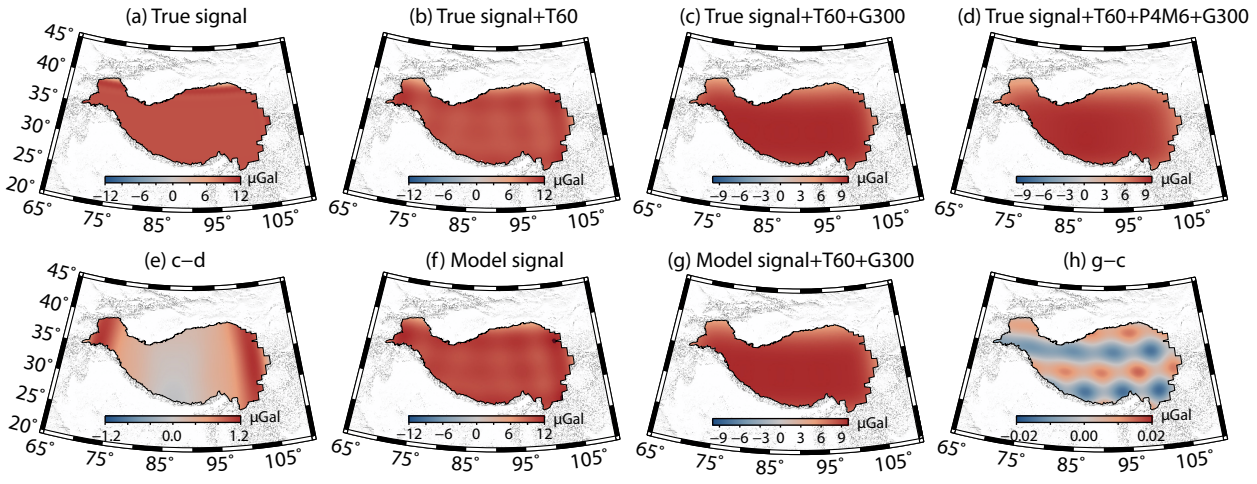

Figure 2. Numerical simulation results. (a) True signal grid. (b) True signal spherical harmonic expansion truncated to 60 order/degree. (c) True signal spherical harmonic expansion truncated to 60 order/degree with Gaussian filtering (300 km). (d) True signal spherical harmonic expansion truncated to 60 order/degree with P4M6 and Gaussian filtering (300 km). (e) Impact of the P4M6 filter. (f) Model signal. (g) Model signal spherical harmonic expansion truncated to 60 order/degree and Gaussian filtered (300 km). (h) Difference between (g) and (c). Note the different scales in each panel. T60, spherical harmonic expansion truncated to 60 order/degree; G300, Gaussian filtering (300 km).

of the area shown in Figure 2a. The difference between Figure 2g and Figure 2c (Figure 2h) was found to be ±0.02 μGal. The real signal was truncated to 60 order/degree and the signal obtained by Gaussian filtering (300 km) was used as the input signal. After the forward modeling method, the root mean square error of the input signal changed from 1.43 μGal to 0.91 μGal. Combined with the small error value of Figure 2h, the restored signal shown in Figure 2f was able to significantly reduce the error caused by the leakage effect.

2.3 Model of Surface Gravity Changes Caused by Vertical Crustal Movement

In Figure 3a, for an individual block unit (upright cuboid), the gravitational force of an external point, $P(x, y, z)$, can be calculated by using Equation (3) (Duan HR et al., 2020):

$$\begin{aligned} &g(x, y, z, a_1, a_2, b_1, b_2, h_1, h_2, \rho) \\ &\quad = -G\rho\left|\left|\left|(\varepsilon - x)\ln[(\eta - y) + q] + (\eta - y)\ln[(\varepsilon - x) + q]\right.\right.\right. \\ &\quad + (\tau - z)\arctan\left[\frac{(\tau - z) + q}{(\varepsilon - x)(\eta - y)}\right]\Bigg|_{a_1}^{a_2}\Bigg|_{b_1}^{b_2}\Bigg|_{h_1}^{h_2}, \end{aligned} \tag{3}$$

where G represents universal gravitational constant, g represents the gravity influence value of upright cuboid on ground points (x, y, z), ρ represents density and $q = \sqrt{(\varepsilon - x)^2 + (\eta - y)^2 + (\tau - z)^2}$.

We used multiple upright cuboids to simulate the crustal model (Figure 3b), and we set the maximum topographic elevation (H_{max}) point of the study area as $Z = 0$. The first upright rectangle on the left corresponds to the partition between the crust and the mantle as Z_2, the corresponding topographic height as H, and the corresponding crustal thickness below the ocean surface as T. The r_0 indicates the difference between H and H_{max}, and its coordinates on the Z-axis are $Z_1 = r_0 = H_{max} - H$ and $Z_2 = Z_1 + T$.

In Figure 3a, the O-XYZ coordinate system is as follows: the ground point is the coordinate origin O, the X-axis points north, the Y-axis points east, and the Z-axis extends down vertically. The range of the upright cuboid in the coordinate system is $[a_1, a_2]$, $[b_1, b_2]$, $[h_1, h_2]$; $k(\varepsilon, \eta, \tau)$ is an arbitrary point inside; and $P(x, y, z)$ is an arbitrary point outside. In Figure 3b, the rectangles filled with diagonal lines represent upright cuboids, which were used to simulate the crustal model with multiple upright cuboids. The bottom surface of each upright cuboid is the partition interface between the crust and the mantle, and the top surface is represented as topographic undulations. The top of the rectangle filled with horizontal dashed lines represents the sea level.

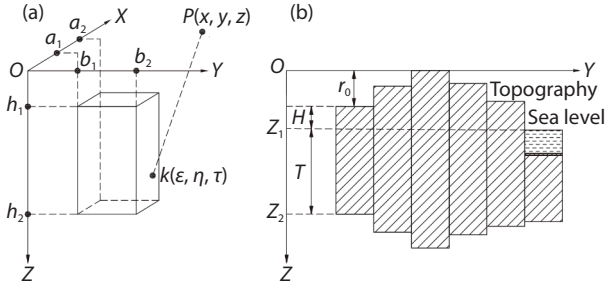

Figure 3. (a) Model of the upright cuboid. (b) Hypothetical crustal model.

The vertical crustal deformation included surface uplift (subsidence) and the uplift (subsidence) of the Moho. We used an upright cuboid to simulate the vertical deformation of the Earth's crust, assuming that the surface rises dz and sinks kdz at the Moho surface, and the gravity change of the calculated point was calculated by Equation (4):

$$\begin{aligned} \Delta g(x, y, z) = &g(x, y, z, a_1, a_2, b_1, b_2, h_1 - \mathrm{d}z, h_2, \rho_{crust}) \\ &- g(x, y, z, a_1, a_2, b_1, b_2, h_1, h_2, \rho_{crust}) \\ &+ g(x, y, z, a_1, a_2, b_1, b_2, h_1, h_2 + k\mathrm{d}z, \rho_{mantle\_crust}) \\ &- g(x, y, z, a_1, a_2, b_1, b_2, h_1, h_2, \rho_{mantle\_crust}), \end{aligned} \tag{4}$$

where ρ_{crust} denotes the density difference between the crust and air, ρ_{mantle_crust} denotes the density difference between the mantle and crust, and k is the vertical deformation coefficient of the surface and the Moho surface.

According to the cumulative gravity effect in the entire study area, the change in gravity caused by the vertical motion of all the upright cuboids (number n) at point $P(x, y, z)$ was calculated by Equation (5) (Duan HR et al., 2020):

$$dg(x, y, z) = \sum_{n=1}^{n} \Delta g_n(x, y, z). \quad (5)$$

2.4 Inversion of the VCDV

To avoid oscillations and jumps in the VCDV distribution, the quadratic difference Laplacian operator was used to constrain the roughness of velocity distribution. The specific inversion algorithm was as follows (Duan HR et al., 2020):

$$\begin{bmatrix} D \\ \lambda L \end{bmatrix} v = \begin{bmatrix} dg \\ 0 \end{bmatrix}, \quad (6)$$

where D is Green's function, that is, $dz = 1$ mm, the gravity change calculated according to Equation (5), v is the VCDV, dg is the gravity change rate caused by the vertical crustal movement, and λ is the smoothing coefficient, which can be determined by using the compromise curve of residuals and roughness. Additionally, L is the Laplace smoothing matrix.

3. Results

3.1 Gravity Change Rate of the TP

As shown in Figure 4, the gravity change rate in the southern part of the TP was negative (with a maximum value of up to approximately −1.2 μGal/a), whereas those in the northern TP and Sichuan Basin were positive (with maximum values of up to ~0.2 and ~0.3 μGal/a, respectively); the gravity change rate in the northeastern TP was nonsignificant (~0.0 μGal/a). To more clearly express these gravity change rates, two regions (A and B in Figure 4) were selected for analysis.

The gravity change trends using data from the three institutions (CSR, JPL, and GFZ) were similar, with a downward trend and corresponding gravity change rate of −0.78 ± 0.12 μGal/a (Figure 5a). The gravity changes in Figure 5b show an upward trend with a corresponding gravity change rate of 0.17 ± 0.02 μGal/a. These gravity changes were mainly influenced by the comprehensive action of various factors (including crustal tectonic movements and hydrological changes; Rodell et al., 2009; Yi S and Sun WK, 2014).

3.2 Gravity Effects Related to Hydrological Factors

The TP is known as the Water Tower of Asia because it is rich in water resources, including glaciers, lake water, SM, SWE, and permafrost. Owing to its unique geographical location, denudation is also severe, and the influence of denudation on gravity change cannot be ignored.

As shown in Figures 6a–6c, changes in glaciers, SM, and lakes play major roles in the hydrological effect, with corresponding maximum gravity effects of 0.42 μGal/a (90.02°E, 36.67°N), 0.31 μGal/a (89.02°E, 22.00°N), and 0.30 μGal/a (86.19°E, 32.17°N). These

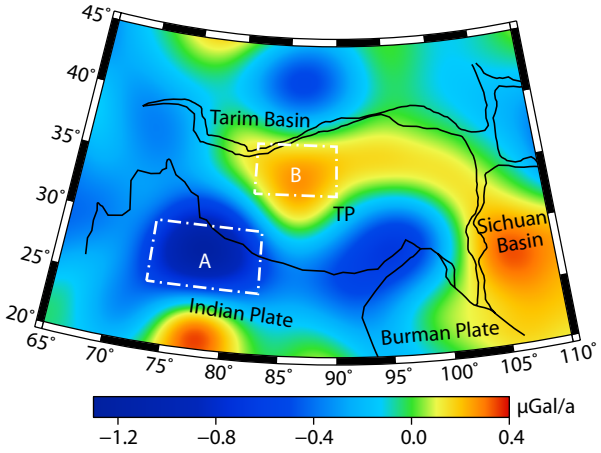

Figure 4. The gravity change rates on the Qinghai–Tibet Plateau (TP). The black plate boundary lines are from Zhang PZ et al. (2013). Regions A and B were selected for further analysis.

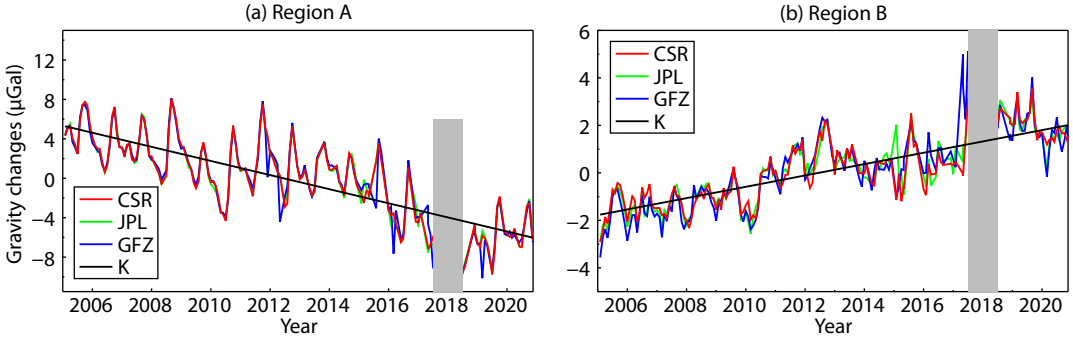

Figure 5. Time series of gravity changes in each subregion (after P4M6 decorrelation filtering and 300-km Gaussian smoothing. (a) Region A; (b) Region B. The red, green, and blue curves represent the gravity change results for the Center for Space Research (CSR), Jet Propulsion Laboratory (JPL), and German Research Centre for Geosciences (GFZ), respectively (in microgal of gravity change), and the straight black line represents the average gravity change rate for the three institutions (in microgal per annum of the average gravity change rate). The gray bars indicate missing raw data.

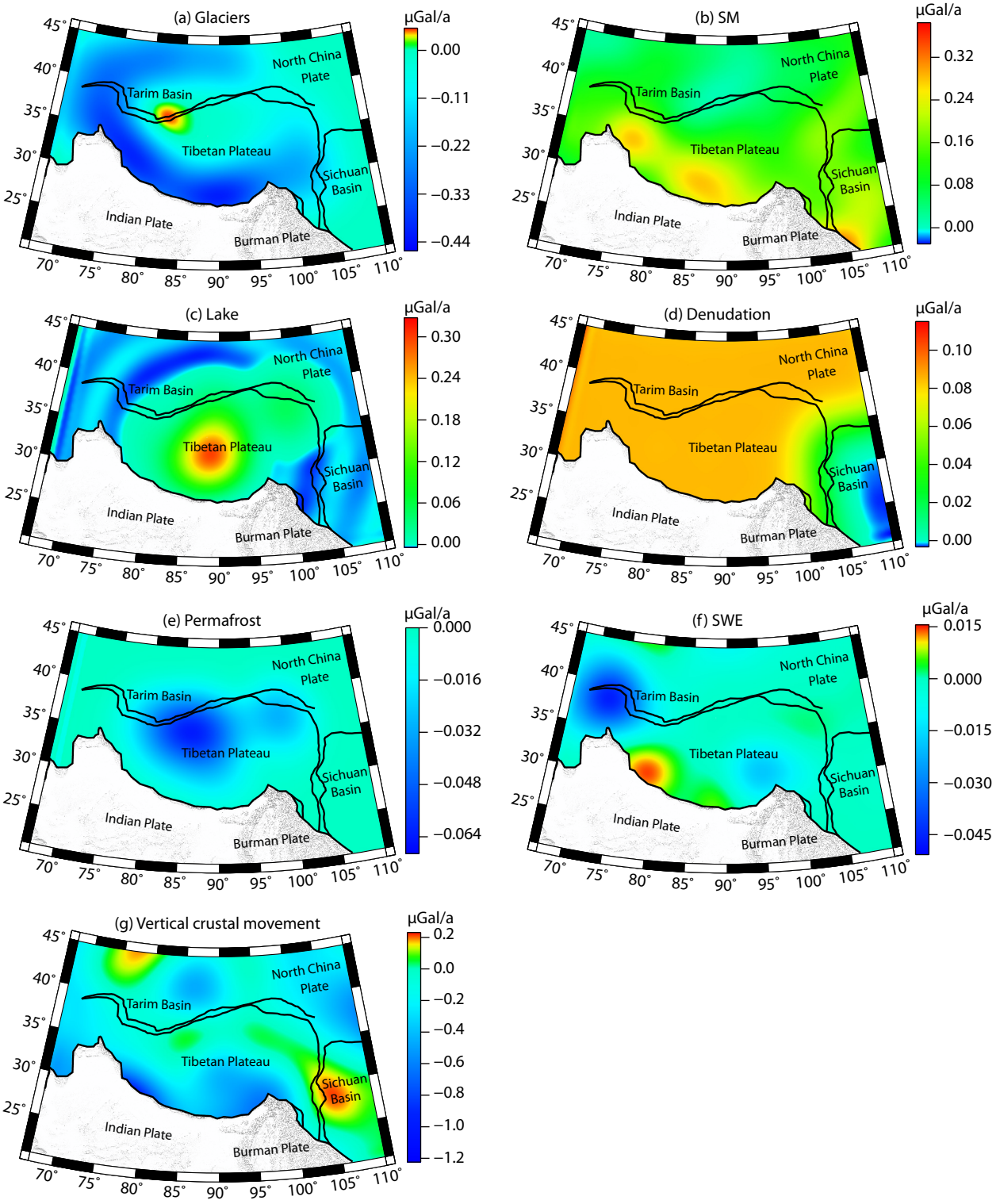

Figure 6. Gravity change rates attributable to hydrological factors and tectonic movement: (a) glaciers; (b) soil moisture (SM); (c) lake water; (d) denudation; (e) permafrost; (f) snow water equivalent (SWE); (g) vertical crustal movement.

effects account for 33.04%, 28.23%, and 23.42% of the total hydrological factors, respectively, based on the relationship $\left|w^i_{\max}\right| / \sum_i \left|w^i_{\max}\right|$, where $w_{\max}$ is the maximum value of the absolute change in gravity for each hydrological factor and i refers to glaciers, SM, lake water, denudation, permafrost, and SWE. The contribution of glaciers to gravity change is mainly concentrated in the Himalayas, the Karakorum Mountains, and the western Kunlun Mountains and is related to glacial melting caused by global warming (Qiu J, 2012). The contribution of SM to the gravity change rate is mainly positive and is concentrated in the south and east of the TP; this distribution is generally consistent with the

trend of equivalent water height of the SM (Rao WL and Sun WK, 2021). The contribution of lake water to gravity change is mainly concentrated in the central TP, with a magnitude of up to ~0.21 to 0.30 μGal/a, which is related to a significant area expansion of numerous lakes (Zhang GQ et al., 2011).

As shown in Figures 6d–6f, changes in denudation, permafrost, and SWE play a relatively minor role in the hydrological effect, with corresponding maximum gravity effects of 0.10 μGal/a (109.83°E, 45.00°N), 0.06 μGal/a (86.19°E, 45.00°N), and 0.05 μGal/a (72.70°E, 30.50°N). These account for 6.72%, 4.96%, and 3.63% of the total hydrological factors, respectively. Westaway (1995) estimated that the total denudation of the TP was 0.90 km^3/a and that the equivalent loss rate of the mass layer was approximately 0.8 mm/a. The terrain of the Sichuan Basin is lower and less affected by denudation. Therefore, the equivalent loss rate of its mass layer was assumed to be 0.0 mm/a in this study. Assuming that the denudation rate follows a simple Bouguer layer, its contribution to the gravity change is approximately 0.09 μGal/a (Sun WK et al., 2009). The contribution of permafrost to the gravity change is mainly concentrated in the north of the TP, where the magnitude reaches −0.06 μGal/a, which is consistent with the trend in the daily active-layer depth variation of ~1.4 cm/a in the same region (Xiang LW et al., 2016). The contribution of SWE to the gravity change is mainly concentrated in the Pamir Plateau, where the magnitude reaches −0.05 μGal/a and is related to snow melting caused by rising temperatures (Yao TD et al., 2012). The overall spatial distribution of gravity change obtained in this study is shown in Figure 6g. The northern region of the TP, the Sichuan Basin, and the Tianshan region show positive gravity changes, with magnitudes reaching ~0.00 to 0.20 μGal/a, and the areas north of the Indian plate and west of the Burman plate show negative gravity changes, with magnitudes reaching approximately −0.40 to −1.00 μGal/a. The gravity changes in other regions (Figure 6g, cyan regions) are relatively small, with values reaching approximately −0.20 to 0.00 μGal/a.

3.3 Crustal Thickness of the TP and Its Periphery

We inverted the crustal thickness of the TP by using the EIGEN6C-4 (European Improved Gravity model of the Earth by New techniques 6C-4) gravity field model according to the method of Moritz (1990). Topographic data were obtained from the ETOP01 global model with a density of 2,670 kg/m^3. A mean crustal thickness of 46 km and a crust–mantle density difference of −470 kg/m^3 were obtained from the CRUST1.0 (global model of the Earth's crustal structure; Sjöberg and Abrehdary, 2021).

The correlation coefficient of crustal thickness and CRUST 1.0 was ~0.86 in this work, which is similar to that of 0.87 reported by Xu C et al. (2017). The results of this study showed that the crustal thickness near Ritu County reaches 70 km. This value is slightly larger than that (68 km) obtained by Zhao GD et al. (2020) and Chen WJ and Tenzer (2017) but lower than that (80 km) of Shin et al. (2015) and Baranov et al. (2018). Within the TP, the average crustal thickness of the Lhasa plate is approximately 69 km, which is much larger than that of the Himalayas (50 km). This thickness is consistent with the results of Stolk et al. (2013) and Chen WJ and Tenzer (2017) and is close to the average crustal thickness of 70 km calculated by Li HO et al. (2008) on the basis of seismic data.

3.4 Inversion of the VCDV Distribution from the TP

To obtain the gravity change rate caused by vertical crustal movement, hydrological factors were deducted from the results obtained in section 3.1. An *XYZ* coordinate system was established in accordance with the information presented in section 2.3. The study area was divided into a grid with a spatial resolution of 1° × 1°, totaling 1,126 upright cuboids. The top and bottom of each upright cuboid were taken as $h_1 = H_{max} - H$ and $h_2 = h_1 + T$, respectively, when the effects of the crustal thickness and topography were considered. Finally, assuming a linear function between the magnitude of the surface uplift and the magnitude of Moho surface subsidence in the TP region, based on the results of Sun WK et al. (2009) and Jiao JS et al. (2019), we took k of Equation (4) as 16, ρ_{crust} as 2,670 kg/m^3, and ρ_{mantle_crust} as 600 kg/m^3. The VCDV distribution was obtained according to the model described in sections 2.3 and 2.4.

Figure 7a shows the VCDV distribution of the TP. The colors from light green to red represent positive vertical deformation and those from light green to blue represent negative vertical deformation. The results showed that the VCDV distribution of the TP has the characteristics of spatial inhomogeneity. The region is dominated by positive vertical deformation except for the Sichuan Basin, the northern TP, and the western Tarim Basin. The positive VCDV is most obvious in the southern TP, with a velocity of ~1.1 mm/a. The VCDV reaches ~0.5 mm/a in the eastern TP and ~0.7 mm/a in the northern Tarim Basin and North China plate. The negative VCDV is most obvious in the Sichuan Basin, with a velocity of approximately −0.4 mm/a. The VCDV is approximately −0.1 mm/a in the northern TP (surrounded by F9, F8, and F1). The VCDV is low between F2 and F3, with a velocity of ~0.0 mm/a. The apparent vertical deformation velocity on the southern margin of the TP may be caused by groundwater depletion in northern India (Liu J et al., 2015).

4. Discussion

4.1 Evidence from GPS and Seismic Activity for the VCDV of the TP

We compared the inversion results in section 3.4 with GPS crustal deformation over 25 years, the distribution of seismic activity over the past 100 years, and fault activity over 10,000 years (see Figure 7). The VCDV of the TP was consistent with the GPS velocity field. The GPS horizontal velocity decreased abruptly whenever it passed through blue areas (e.g., Q1, Q2, and Q3 in Figure 7b). In region Q1, the GPS horizontal velocity was ~31.4 mm/a when it crossed the southern margin of the TP and was ~15.9 mm/a at the Tarim Basin. In region Q2, the GPS horizontal velocity was ~24.1 mm/a when it crossed F4 and was ~5.0 mm/a when it reached F2. In region Q3, the GPS horizontal velocity was ~24.1 mm/a when it crossed the southeastern margin of the TP and was ~9.0 mm/a when it reached the eastern Sichuan Basin. We assumed that the tectonic deformation of the TP was continuous and that horizontal convergence (divergence) volume flux compensated for the vertical uplift (subsidence) of the region. According to the relationships among the horizontal velocity differences, the VCDV differences, and the distances between blocks, the constants between blocks could be determined (Rao WL and Sun WK, 2021). We chose A′ (79.80° to 82.83°, 30.38° to

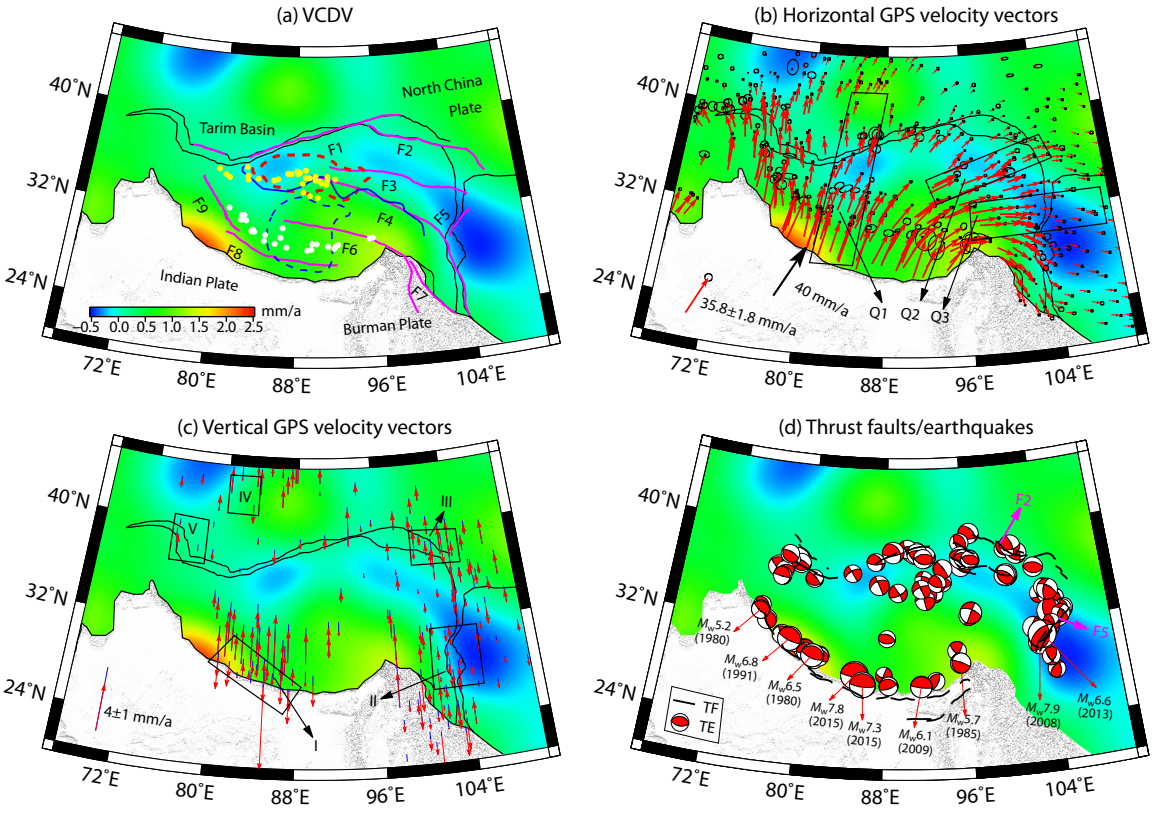

Figure 7. The vertical crustal deformation velocity (VCDV) distribution of the Qinghai–Tibet Plateau (TP). (a) The VCDV distribution, where the white dots represent ultrapotassic + adakitic magmatism (~30 to 9 Ma), the yellow dots represent potassic (+ crustal) magmatism (~15 to 0 Ma), the red dashed line represents the northwestern Tibet low wave speed (low-V) zone, the solid blue line represents the convectively removed lithosphere (mostly Tibetan), the dashed blue line represents the underthrusting front of the Indian lithosphere, and the magenta lines represent strike-slip faults. (b) Distribution of the VCDV and the horizontal global positioning system (GPS) velocity under the Eurasian plate (Wang M and Shen ZK, 2020), where the red arrows indicate the GPS horizontal velocity with a 70% error ellipse confidence level. The Q1, Q2 and Q3 in Figure b represent the three subregions of the Tibetan Plateau (See three black boxes). (c) Distribution of the VCDV and the vertical GPS velocity, where the red arrows indicate the vertical velocity and the blue lines indicate the error. The Ⅰ, Ⅱ, Ⅲ, Ⅳ and Ⅴ in Figure c represent the five subregions of the Tibetan Plateau(See five black boxes, the same as follow). (d) Distribution of the VCDV and the thrust faults and earthquakes, where TE denotes a thrust earthquake and TF denotes a thrust fault. Data on the focal mechanism solutions were obtained for the years 1976 to 2013 (magnitude $\geq$ 5.0 M_w and depth of 10–279 km, from http://neic.usgs.gov/, http://data.earthquake.cn and previous studies, e.g., Deng YH et al., 2018). F1, Altun Fault Zone; F2, Qilian–Haiyuan Fault Zone; F3, Kunlun Fault Zone; F4, Xianshui River Fault Zone; F5, Longmenshan Fault Zone; F6, Bangongcuo–Jiali Fault Zone; F7, Red River Fault Zone; F8, Himalayan active belt; F9, Karakorum Fault Zone.

32.61°, 19.60 mm/a, 0.64 mm/a; the data types are longitude, latitude, GPS horizontal velocity, and VCDV and are the same below), B′ (93.07° to 96.41°, 27.62° to 31.59°, 22.12 mm/a, 1.02 mm/a), C′ (84.52° to 86.38°, 35.46° to 37.41°, 16.18 mm/a, −0.11 mm/a), and D′ (99.07° to 100.81°, 34.46° to 36.80°, 12.35 mm/a, −0.08 mm/a). The constant between regions A′ and B′ was 0.11×10^{-5}, which was close to the constant 0.73×10^{-5} between regions C′ and region D′. This result indicates that the VCDV distribution was consistent with the GPS horizontal velocity distribution.

In addition, we found that the VCDV of the TP was consistent with the GPS vertical velocity distribution (Pan YJ et al., 2018; Figure 7c). The differences between the results and the GPS vertical velocities for all subregions in Figure 6c were less than ±0.13 mm/a (see Table 1). These results showed that the VCDV distribution was consistent with the GPS (horizontal, vertical) velocity distribution.

The VCDV distribution of the TP was also consistent with the distribution of thrust earthquakes and faults. The VCDV of the southern area was positive in areas where many thrust earthquakes had occurred (e.g., M_w 5.2 in 1980, M_w 6.5 in 1980, M_w 5.7 in 1985, M_w 6.8 in 1991, M_w 6.1 in 2009, M_w 7.3 in 2015, and M_w 7.8 in 2015). The southern margin of the TP contains a number of thrust faults (black lines in Figure 7d). The VCDV around F2 was also positive

Table 1. Comparison of the global positioning system (GPS) vertical velocities and the vertical crustal deformation velocities (VCDV).

Region	VCDV (mm/a)	GPS (mm/a)	Difference (mm/a)
Ⅰ	0.753 ± 0.151	0.756 ± 1.851	±0.003
Ⅱ	−0.147 ± 0.022	−0.210 ± 0.731	±0.063
Ⅲ	0.703 ± 0.056	0.744 ± 1.351	±0.041
Ⅵ	0.633 ± 0.133	0.555 ± 1.450	±0.078
Ⅴ	0.184 ± 0.120	0.310 ± 0.715	±0.126

and reflects many thrust earthquakes and fault zones. However, even though multiple thrust earthquakes have occurred near F5, the VCDV in this area is negative, implying that the resolution of the results is not sufficient to recognize the linear tectonic uplift of the fault zone.

4.2 Lithospheric Activity and the VCDV of the TP

For 50 Ma, the Indian plate has been compressing (and subsequently subducting beneath) the TP in a north–east direction, forming multiple, nearly east–west stretched tectonic belts within the TP. Simultaneously, mantle convection beneath the lithosphere has caused a shortening and thickening of the crust (England and Houseman, 1989). We considered the correspondence between the vertical deformation distribution and the lithospheric activity in the southern, central, and northern regions of the TP.

The positive VCDV of the Himalayan belt was mainly caused by strong deformation of the crustal lithosphere. In the southern TP, continent–continent collision has resulted in lithospheric extrusion and deformation, further forming a series of domed tectonic belts (Fu JG et al., 2017).

The Himalayan tectonic belt is dotted with pale granites (46–10 Ma) along a length of ~3,000 km (Wu FY et al., 2020; Huang F et al., 2021), corresponding to the distribution of positive VCDV in this region. In the central TP, the positive VCDV of the Lhasa–Qiangtang tectonic belt corresponds to lithospheric demolition and melting and the distribution of ultrapotassic and adakitic magmatism (Xu WC et al., 2015). In addition, the distribution of positive VCDV corresponds to a lithospheric demolition and melting phenomenon inferred from seismic stratigraphy data (Chen M et al., 2017). The negative VCDV in the northern TP is related to recent potassic (+ crustal) magmatism activity. In the northern TP, a narrow, low-wave speed zone exists at a depth of 80 km, corresponding to both recent potassic (+ crustal) magmatism (Chen M et al., 2017) and a negative VCDV (Figure 7a).

4.3 Influence of Hydrology, Crustal Thickness, and Topography

To analyze the influence of various additional gravity effects on the VCDV of the TP, the VCDV distribution generated by pure tectonic movement (see Figure 7a) was used as a reference. From Figures 8a and 8a′, it is evident that the maximum influence of hydrology on the VCDV is approximately −0.4 mm/a (in the northwest) to 1.0 mm/a (in the central region), which can be primarily attributed to changes in the glaciers, lake water, and SM. Figure 8b shows the VCDV distribution that considers crustal thickness of 60 km (Duan HR et al., 2020). From Figures 8b and 8b′, it is evident that the influence of the degree of crustal thickness on the VCDV is approximately −0.06 to 0.06 mm/a. The effect is most pronounced for the southern TP, where the value ranges from ~0.03 to 0.06 mm/a, primarily because the simulated crustal thickness of 60 km at this point is inconsistent with the true value. From Figures 8c and 8c′, it is evident that the influence of the degree of topography on the VCDV is approximately −0.03 to 0.01 mm/a and is dependent on altitude. High-altitude areas in the central TP are greatly affected by the topographic effect, whereas the surrounding low-altitude areas are less affected. When the altitude is between 0 and 3,000 m, the influence is approximately −0.01 mm/a, but when the altitude is between 4,000 and 5,000 m, the influence reaches approximately −0.03 mm/a.

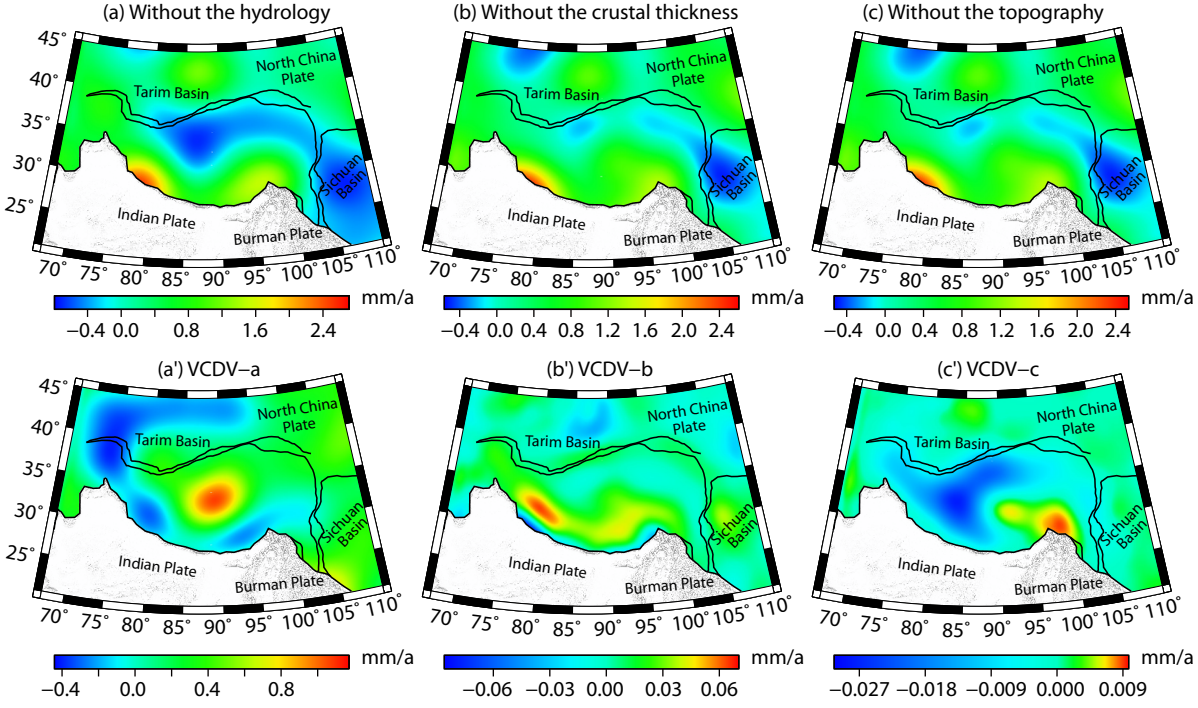

Figure 8. Analysis of factors influencing the vertical crustal deformation velocity (VCDV). Without considering the (a) hydrology, (b) crustal thickness, and (c) topography. With the influence of the (a′) hydrology, (b′) crustal thickness, and (c′) topography.

5. Conclusions

The TP is in a state of motion owing to the collision and extrusion of the Indian and Eurasian plates. To obtain the VCDV distribution characteristics of the TP, we removed hydrological factors from the GRACE data to obtain the gravity change of the vertical crustal movement. Furthermore, the VCDV was inverted by using an upright cuboid model in which the crustal thickness and topography were considered. The major conclusions drawn from the findings of this study are as follows:

(1) The gravity change of the TP shows that uplift occurs in most areas, with a few areas experiencing subsidence. The VCDV of the southern, eastern, and northern TP is approximately 1.1 mm/a, 0.5 mm/a, and −0.1 mm/a, respectively. The VCDV distribution of the TP is consistent with the distribution of crustal deformation, thrust earthquakes and faults, and regional lithospheric activity.

(2) Among the hydrological, crustal, and topographical factors that affect the velocity of vertical crustal movement, hydrology is the most significant, followed by crustal thickness and then topography. The main hydrological factors affecting the gravity change are glaciers, SM, and lake water, which account for up to 84% of the total hydrology.

The results of this study have a far-reaching impacts on geomorphic evolution and the occurrence of various geological disasters. At the same time, there are also some problems in our study, such as the consumption of groundwater, heterogeneity of underground density, denudation and horizontal crustal movement, which are not considered. More data types with higher resolutions are required to estimate the effects of these factors in the future.

Acknowledgments

The authors thank the agencies for providing free GRACE (http://icgem.gfz-potsdam.de), GLDAS (https://hydro1.gesdisc.eosdis.nasa.gov/data/GLDAS), and CPC (https://psl.noaa.gov/data/gridded/data.gpcc.html) data. The figures were plotted using Generic Mapping Tool (GMT) software (Wessel et al., 2013). This research was financially supported by the State Key Laboratory of Geodesy and Earth's Dynamics (Grant No. SKLGED2022-5-2), the Innovation Academy for Precision Measurement Science and Technology, the National Natural Science Foundation of China (Grant Nos. 41304013, 41967038), the Natural Science Foundation of Guangdong Province (Grant No. 2021A1515011487), and the Guangdong University of Petrochemical Technology Talent Recruitment (No. 520130). The China Earthquake Networks Center, National Earthquake Data Center (http://data/earthquake.cn), is acknowledged for data support. We also thank the two anonymous reviewers for their comments.

References

An, Z. S., Kutzbach, J. E., Prell, W. L., and Porter, S. C. (2001). Evolution of Asian monsoons and phased uplift of the Himalaya-Tibetan Plateau since Late Miocene times. *Nature*, *411*(6833), 62–66. https://doi.org/10.1038/35075035

Baranov, A., Bagherbandi, M., and Tenzer, R. (2018). Combined gravimetric-seismic Moho model of Tibet. *Geosciences*, *8*(12), 461. https://doi.org/10.3390/geosciences8120461

Braitenberg, C., Zadro, M., Fang, J., Wang, Y., and Hsu, H. T. (2000). The gravity and isostatic Moho undulations in Qinghai-Tibet plateau. *J. Geodyn.*, *30*(5), 489–505. https://doi.org/10.1016/S0264-3707(00)00004-1

Chen, J. L., Wilson, C. R., Tapley, B. D., Longuevergne, L., Yang, Z. L., and Scanlon, B. R. (2010). Recent La Plata basin drought conditions observed by satellite gravimetry. *J. Geophys. Res.*, *115*(D22), D22108. https://doi.org/10.1029/2010JD014689

Chen, J. L., Wilson, C. R., Li, J., and Zhang, Z. Z. (2015). Reducing leakage error in GRACE-observed long-term ice mass change: a case study in West Antarctica. *J. Geod.*, *89*(9), 925–940. https://doi.org/10.1007/s00190-015-0824-2

Chen, M., Niu, F. L., Tromp, J., Lenardic, A., Lee, C. T. A., Cao, W. R., and Ribeiro, J. (2017). Lithospheric foundering and underthrusting imaged beneath Tibet. *Nat. Commun.*, *8*, 15659. https://doi.org/10.1038/ncomms15659

Chen, W. J., and Tenzer, R. (2017). Moho modeling in spatial domain: a case study under Tibet. *Adv. Space Res.*, *59*(12), 2855–2869. https://doi.org/10.1016/j.asr.2017.03.015

Dai, F. C., Xu, C., Yao, X., Xu, L., Tu, X. B., and Gong, Q. M. (2011). Spatial distribution of landslides triggered by the 2008 Ms 8.0 Wenchuan earthquake, China. *J. Asian Earth Sci.*, *40*(4), 883–895. https://doi.org/10.1016/j.jseaes.2010.04.010

Deng, Y. H., Cheng, H. H., Zhang, B., Zhang, H., and Shi, Y. L. (2018). Establishment of the fault slip model for large historical earthquakes and its influence on co-seismic calculations: an example of the M_S8.5 Haiyuan earthquake in 1920. . *Chinese J. Geophys.* (*in Chinese*), *61*(3), 975–987. https://doi.org/10.6038/cjg2018L0096

Dewey, J. F., and Burke, K. C. A. (1973). Tibetan, variscan, and precambrian basement reactivation: products of continental collision. *J. Geol.*, *81*(6), 683–692. https://doi.org/10.1086/627920

Duan, H. R., Zhang, Y. Z., Xu, H. J., and Yao, W. Q. (2011). Velocity of crustal vertical movement computed by using GRACE data in China's western region. *Prog. Geophys.* (*in Chinese*), *26*(4), 1201–1205. https://doi.org/10.3969/j.issn.1004-2903.2011.04.009

Duan, H. R., Kang, M. Z., Wu, S. Y., Chen, L. K., and Jiao, J. S. (2020). Uplift rate of the Tibetan Plateau constrained by GRACE time-variable gravity field. *Chinese J. Geophys.* (*in Chinese*), *63*(12), 4345–4360. https://doi.org/10.6038/cjg2020O0262

England, P., and Houseman, G. (1989). Extension during continental convergence, with application to the Tibetan Plateau. *J. Geophys. Res.: Solid Earth*, *94*(B12), 17561–17579. https://doi.org/10.1029/JB094iB12p17561

England, P., and Molnar, P. (1990). Right-lateral shear and rotation as the explanation for strike-slip faulting in eastern Tibet. *Nature*, *344*(6262), 140–142. https://doi.org/10.1038/344140a0

Erkan, K., Shum, C. K., Wang, L., Guo, J. Y., Jekeli, C., Lee, H., Panero, W. R., Duan, J. B., Huang, Z. W., and Wang, H. S. (2011) Geodetic constraints on the Qinghai-Tibetan Plateau present-day geophysical processes. *Terr. Atmos. Ocean. Sci.*, *22*, 241–253. https://doi.org/10.3319/TAO.2010.09.27.01(TibXS

Feng, Z. M., Li, W. J., Li, P., and Xiao, C. W. (2020). Relief degree of land surface and its geographical meanings in the Qinghai-Tibet Plateau, China. *Acta Geogr. Sin.* (*in Chinese*), *75*(7), 1359–1372. https://doi.org/10.11821/dlxb202007003

Fu, J. G., Li, G. M., Wang, G. H., Huang, Y., Zhang, L. K., Dong, S. L., and Liang, W. (2017). First field identification of the Cuonadong dome in southern Tibet: implications for EW extension of the North Himalayan gneiss dome. *Int. J. Earth Sci.*, *106*(5), 1581–1596. https://doi.org/10.1007/s00531-016-1368-2

Gardner, A. S., Moholdt, G., Cogley, J. G., Wouters, B., Arendt, A. A., Wahr, J., Berthier, E., Hock, R., Pfeffer, W. T., … Paul, F. (2013). A reconciled estimate of glacier contributions to sea level rise: 2003 to 2009. *Science*, *340*(6134), 852–857. https://doi.org/10.1126/science.1234532

Geruo, A., Wahr, J., and Zhong, S. J. (2013). Computations of the viscoelastic response of a 3-D compressible Earth to surface loading: an application to Glacial Isostatic Adjustment in Antarctica and Canada. *Geophys. J. Int.*, *192*(2), 557–572. https://doi.org/10.1093/gji/ggs030

Han, S. C., Shum, C. K., Bevis, M., Ji, C., and Kuo, C. Y. (2006). Crustal dilatation observed by GRACE after the 2004 Sumatra-Andaman earthquake. *Science*, *313*(5787), 658–662. https://doi.org/10.1126/science.1128661

Hao, M., Wang, Q. L., Shen, Z. K., Cui, D. X., Ji, L. Y., Li, Y. H., and Qin, S. L. (2014). Present day crustal vertical movement inferred from precise leveling data in eastern margin of Tibetan Plateau. *Tectonophysics*, *632*, 281–292. https://

doi.org/10.1016/j.tecto.2014.06.016

He, C. S. (2019). Uplift mechanism of the world's largest continental plateau in Tibet. *Acta Geol. Sin. - Engl. Ed.*, *93*(S1), 110. https://doi.org/10.1111/1755-6724.13971

Huang, F., Bai, R. X., Deng, G. X., Liu, X. C., and Li, X. H. (2021). Barium isotope evidence for the role of magmatic fluids in the origin of Himalayan leucogranites. *Sci. Bull.*, *66*(22), 2329–2336. https://doi.org/10.1016/j.scib.2021.07.020

Jiao, J. S., Zhang, Y. Z., Yin, P., Zhang, K. N., Wang, Y. P., and Bilker-Koivula, M. (2019). Changing Moho beneath the Tibetan Plateau revealed by GRACE observations. *J. Geophys. Res.*: *Solid Earth*, *124*(6), 5907–5923. https://doi.org/10.1029/2018JB016334

Li, H. O., Xu, X. W., and Jiang, M. (2008). Deep dynamical processes in the central-southern Qinghai-Tibet Plateau—receiver functions and travel-time residuals analysis of north Hi-Climb. *Sci. China Ser. D*: *Earth Sci.*, *51*(9), 1297–1305. https://doi.org/10.1007/s11430-008-0096-2

Li, P., Zhu, A. Y., Han, W., and Li, M. (2012). Numerical simulation of geodynamic problems—take present uplift of Qinghai-Tibet Plateau as example. *Seismol. Geomag. Obser. Res.* (*in Chinese*), *33*(5), 1–6. https://doi.org/10.3969/j.issn.1003-3246.2012.05/06.001

Liang, S. M., Gan, W. J., Shen, C. Z., Xiao, G. R., Liu, J., Chen, W. T., Ding, X. G., and Zhou, D. M. (2013). Three-dimensional velocity field of present-day crustal motion of the Tibetan Plateau derived from GPS measurements. *J. Geophys. Res.*: *Solid Earth*, *118*(10), 5722–5732. https://doi.org/10.1002/2013JB010503

Liu, J., Fang, J., Li, H. L., Cui, R. H., and Chen, M. (2015). Secular variation of gravity anomalies within the Tibetan Plateau derived from GRACE data. *Chinese J. Geophys.* (*in Chinese*), *58*(10), 3496–3506. https://doi.org/10.6038/cjg20151006

Loomis, B. D., Rachlin, K. E., Wiese, D. N., Landerer, F. W., and Luthcke, S. B. (2020). Replacing GRACE/GRACE-FO C_{30} with satellite laser ranging: impacts on Antarctic Ice Sheet mass change. *Geophys. Res. Lett.*, *47*(3), e2019GL085488. https://doi.org/10.1029/2019GL085488

Mohamed, A., Sultan, M., Ahmed, M., Yan, E., and Ahmed, E. (2017). Aquifer recharge, depletion, and connectivity: inferences from GRACE, land surface models, and geochemical and geophysical data. *Geol. Soc. Am. Bull.*, *129*(5-6), 534–546. https://doi.org/10.1130/B31460.1

Molnar, P., and Tapponnier, P. (1975). Cenozoic tectonics of Asia: effects of a continental collision: features of recent continental tectonics in Asia can be interpreted as results of the India-Eurasia collision. *Science*, *189*(4201), 419–426. https://doi.org/10.1126/science.189.4201.419

Moritz, H. (1990). The inverse Vening Meinesz problem in isostasy. *Geophys. J. Int.*, *102*(3), 733–738. https://doi.org/10.1111/j.1365-246X.1990.tb04591.x

Oelke, C., and Zhang, T. J. (2007). Modeling the active-layer depth over the Tibetan Plateau. *Arct. Antarct. Alp. Res.*, *39*(4), 714–722. https://doi.org/10.1657/1523-0430(06-200)[OELKE]2.0.CO;2

Pan, Y. J., Shen, W. B., Shum, C. K., and Chen, R. Z. (2018). Spatially varying surface seasonal oscillations and 3-D crustal deformation of the Tibetan Plateau derived from GPS and GRACE data. *Earth Planet. Sci. Lett.*, *502*, 12–22. https://doi.org/10.1016/j.epsl.2018.08.037

Qiao, B. J., Zhu, L. P., and Yang, R. M. (2019). Temporal-spatial differences in lake water storage changes and their links to climate change throughout the Tibetan Plateau. *Remote Sens. Environ.*, *222*, 232–243. https://doi.org/10.1016/j.rse.2018.12.037

Qiu, J. (2010). Measuring the meltdown. *Nature*, *468*(7321), 141–142. https://doi.org/10.1038/468141a

Qiu, J. (2012). Tibetan glaciers shrinking rapidly. *Nature News*., 15 July 2012. https://doi.org/10.1038/nature.2012.11010

Rao, W. L., and Sun, W. K. (2021). Moho interface changes beneath the Tibetan Plateau based on GRACE data. *J. Geophys. Res.*: *Solid Earth*, *126*(2), e2020JB020605. https://doi.org/10.1029/2020JB020605

Rao, W. L., and Sun, W. K. (2022). Runoff variations in the Yangtze River Basin and sub-basins based on GRACE, hydrological models, and in-situ data. *Earth Planet. Phys.*, *6*(3), 228–240. https://doi.org/10.26464/epp2022021

Rodell, M., Houser, P. R., Jambor, U., Gottschalck, J., Mitchell, K., Meng, C. J., Arsenault, K., Cosgrove, B., Radakovich, J., … Toll, D. (2004). The global land data assimilation system. *Bull. Amer. Meteor. Soc.*, *85*(3), 381–394. https://doi.org/10.1175/BAMS-85-3-381

Rodell, M., Velicogna, I., and Famiglietti, J. S. (2009). Satellite-based estimates of groundwater depletion in India. *Nature*, *460*(7258), 999–1002. https://doi.org/10.1038/nature08238

Shen, Y., Wang, Q. Y., Rao, W. L., and Sun, W. K. (2022). Spatial distribution characteristics and mechanism of nonhydrological time-variable gravity in China contient. *Earth Planet. Phys.*, *6*(1), 96–107. https://doi.org/10.26464/epp2022009

Shin, Y. H., Shum, C. K., Braitenberg, C., Lee, S. M., Na, S. H., Choi, K. S., Hsu, H., Park, Y. S., and Lim, M. (2015). Moho topography, ranges and folds of Tibet by analysis of global gravity models and GOCE data. *Sci. Rep.*, *5*, 11681. https://doi.org/10.1038/srep11681

Sjöberg, L. E., and Abrehdary, M. (2021). The uncertainty of CRUST1.0: Moho depth and density contrast models. *J. Appl. Geod.*, *15*(2), 143–152. https://doi.org/10.1515/jag-2020-0049

Steffen, H., Petrovic, S., Müller, J., Schmidt, R., Wünsch, J., Barthelmes, F., and Kusche, J. (2009). Significance of secular trends of mass variations determined from GRACE solutions. *J. Geodyn.*, *48*(3-5), 157–165. https://doi.org/10.1016/j.jog.2009.09.029

Stolk, W., Kaban, M., Beekman, F., Tesauro, M., Mooney, W. D., and Cloetingh, S. (2013). High resolution regional crustal models from irregularly distributed data: application to Asia and adjacent areas. *Tectonophysics*, *602*, 55–68. https://doi.org/10.1016/j.tecto.2013.01.022

Sun, W. K., Wang, Q., Li, H., Wang, Y., Okubo, S., Shao, D. S., Liu, D. Z., and Fu, G. Y. (2009). Gravity and GPS measurements reveal mass loss beneath the Tibetan Plateau: geodetic evidence of increasing crustal thickness. *Geophys. Res. Lett.*, *36*(2), L02303. https://doi.org/10.1029/2008GL036512

Sun, Y., Riva, R., and Ditmar, P. (2016). Optimizing estimates of annual variations and trends in geocenter motion and J_2 from a combination of GRACE data and geophysical models. *J. Geophys. Res.*: *Solid Earth*, *121*(11), 8352–8370. https://doi.org/10.1002/2016JB013073

Velicogna, I. (2009). Increasing rates of ice mass loss from the Greenland and Antarctic ice sheets revealed by GRACE. *Geophys. Res. Lett.*, *36*(19), L19503. https://doi.org/10.1029/2009GL040222

Wang, H. S., Wu, P., and Wang, Z. Y. (2006). An approach for spherical harmonic analysis of non-smooth data. *Comput. Geosci.*, *32*(10), 1654–1668. https://doi.org/10.1016/j.cageo.2006.03.004

Wang, M., and Shen, Z. K. (2020). Present-day crustal deformation of continental China derived from GPS and its tectonic implications. *J. Geophys. Res.*: *Solid Earth*, *125*(2), e2019JB018774. https://doi.org/10.1029/2019JB018774

Wang, Q., Zhang, P. Z., Freymueller, J. T., Bilham, R., Larson, K. M., Lai, X. A., You, X. Z., Niu, Z. J., Wu, J. C., … Chen, Q. Z. (2001). Present-day crustal deformation in China constrained by global positioning system measurements. *Science*, *294*(5542), 574–577. https://doi.org/10.1126/science.1063647

Wessel, P., Smith, W. H. F., Scharroo, R., Luis, J., and Wobbe, F. (2013). Generic mapping tools: improved version released. *Eos Trans. AGU*, *94*(45), 409–410. https://doi.org/10.1002/2013EO450001

Westaway, R. (1995). Crustal volume balance during the India-Eurasia collision and altitude of the Tibetan Plateau: a working hypothesis. *J. Geophys. Res.*: *Solid Earth*, *100*(B8), 15173–15192. https://doi.org/10.1029/95JB01310

Wu, F. Y., Liu, X. C., Liu, Z. C., Wang, R. C., Xie, L., Wang, J. M., Ji, W. Q., Yang, L., Liu, C., … He, S. X. (2020). Highly fractionated Himalayan leucogranites and associated rare-metal mineralization. *Lithos*, *352–353*, 105319. https://doi.org/10.1016/j.lithos.2019.105319

Xiang, L. W., Wang, H. S., Steffen, H., Wu, P., Jia, L. L., Jiang, L. M., and Shen, Q. (2016). Groundwater storage changes in the Tibetan Plateau and adjacent areas revealed from GRACE satellite gravity data. *Earth Planet. Sci. Lett.*, *449*, 228–239. https://doi.org/10.1016/j.epsl.2016.06.002

Xing, L. L., Sun, W. K., Li, H., and Yang, G. L. (2011). Present-day crust thickness increasing beneath the Qinghai-Tibetan Plateau by using geodetic data at Lhasa station. *Acta Geodaet. Cartogr. Sin.* (in Chinese), *40*(1), 41–44, 58.

Xu, C., Liu, Z. W., Luo, Z. C., Wu, Y. H., and Wang, H. H. (2017). Moho topography

of the Tibetan Plateau using multi-scale gravity analysis and its tectonic implications. *J. Asian Earth Sci.*, *138*, 378–386. https://doi.org/10.1016/j.jseaes.2017.02.028

Xu, W. C., Zhang, H. F., Luo, B. J., Guo, L., and Yang, H. (2015). Adakite-like geochemical signature produced by amphibole-dominated fractionation of arc magmas: an example from the Late Cretaceous magmatism in Gangdese belt, south Tibet. *Lithos*, *232*, 197–210. https://doi.org/10.1016/j.lithos.2015.07.001

Yao, T. D., Thompson, L., Yang, W., Yu, W. S., Gao, Y., Guo, X. J., Yang, X. X., Duan, K. Q., Zhao, H. B., … Joswiak, D. (2012). Different glacier status with atmospheric circulations in Tibetan Plateau and surroundings. *Nat. Climate Change*, *2*(9), 663–667. https://doi.org/10.1038/nclimate1580

Ye, H., Yi, G. H., Zhang, T. B., Zhou, X. B., Li, J. J., Bie, X. J., Shen, Y. L., and Yang, Z. L. (2020). Spatiotemporal variations of snow cover in the Qinghai-Tibetan Plateau from 2000 to 2019. . *Resour Sci.* (*in Chinese*), *42*(12), 2434–2450. https://doi.org/10.18402/resci.2020.12.14

Yi, S., and Sun, W. K. (2014). Evaluation of glacier changes in high-mountain Asia based on 10 year GRACE RL05 models. *J. Geophys. Res.*: *Solid Earth*, *119*(3), 2504–2517. https://doi.org/10.1002/2013JB010860

Yi, S., Freymueller, J. T., and Sun, W. K. (2016). How fast is the middle-lower crust flowing in eastern Tibet? A constraint from geodetic observations. *J. Geophys. Res.*: *Solid Earth*, *121*(9), 6903–6915. https://doi.org/10.1002/2016JB013151

Zhang, G. Q., Xie, H. J., Kang, S. C., Yi, D. H., and Ackley, S. F. (2011). Monitoring lake level changes on the Tibetan Plateau using ICESat altimetry data (2003–2009). *Remote Sens. Environ.*, *115*(7), 1733–1742. https://doi.org/10.1016/j.rse.2011.03.005

Zhang, P. Z., Deng, Q. D., Zhang, Z. Q., and Li, H. B. (2013). Active faults, earthquake hazards and associated geodynamic processes in continental China. *Sci. Sin. Terr.* (*in Chinese*), *43*(10), 1607–1620. https://doi.org/10.1360/zd-2013-43-10-1607

Zhao, G. D., Liu, J. X., Chen, B., Kaban, M. K., and Zheng, X. Y. (2020). Moho beneath Tibet based on a joint analysis of gravity and seismic data. *Geochem. Geophys. Geosyst.*, *21*(2), e2019GC008849. https://doi.org/10.1029/2019GC008849